



Functional and eco-friendly nanocomposite kaolinite/ZnO with high photocatalytic activity



Kateřina Mamulová Kutláková^a, Jonáš Tokarský^{a,b,*}, Pavlína Peikertová^a

^a Nanotechnology Centre, VŠB – Technical University of Ostrava, 17. listopadu 15, 708 33 Ostrava, Czech Republic

^b IT4Innovations Centre of Excellence, VŠB – Technical University of Ostrava, 17. listopadu 15, 708 33 Ostrava, Czech Republic

ARTICLE INFO

Article history:

Received 25 April 2014

Received in revised form 23 June 2014

Accepted 7 July 2014

Available online 15 July 2014

Keywords:

Kaolinite

ZnO

Photoactivity

Nanocomposite

ABSTRACT

Highly photoactive nanocomposites kaolinite/ZnO with various amounts of ZnO nanoparticles (10 wt.%, 30 wt.%, and 50 wt.%) were prepared using simple hydrothermal method. Calcination of the nanocomposites at 600 °C led to the kaolinite–metakaolinite phase transformation, to further growth of ZnO crystallites, and to significant increase of photodegradation activity. The nanocomposites were studied using X-ray fluorescence spectroscopy, X-ray powder diffraction, Fourier transform infrared, diffuse reflectance and photoluminescence spectroscopies, scanning and transmission electron microscopies, BET analysis, and molecular modeling using empirical force field. Photodegradation activity was evaluated by the discoloration of Acid Orange 7 aqueous solution under UV irradiation. Leaching tests confirmed strong interaction between kaolinite matrix and ZnO nanoparticles, and, therefore, high stability of prepared nanocomposites.

© 2014 Elsevier B.V. All rights reserved.

1. Introduction

Zinc oxide (ZnO), a low-cost semiconductor having large band gap ~ 3.3 eV, belongs to the most studied and commonly used nanomaterials, mainly for its good photocatalytic, piezoelectric and antibacterial properties. ZnO nanoparticles (NPs) can be prepared via various methods (hydrothermal synthesis [1–4], coprecipitation method [5,6], sol–gel method [7,8], non-aqueous solution method [9], photolysis [10], solid state mixing of precursors [11], thermal decomposition of precursor [12], microwave assisted synthesis [13], vapor deposition techniques [14]) using various precursors (zinc chloride + sodium hydroxide [3,4,8,15], zinc chloride + ammonia [1,2], zinc acetate + sodium hydroxide [3,16–18], zinc acetate + lithium hydroxide [19], zinc acetate + octadecylamine [9], zinc acetate + oxalic acid [6], zinc acetate + acetic acid [20], zinc acetate + hydrogen peroxide [10], zinc nitrate + sodium hydroxide [3], zinc nitrate + citric acid [11], zinc nitrate + ammonia [2], zinc sulfate + sodium hydroxide [3], zinc sulfate + sodium carbonate [21]) and it is known that different reaction conditions give rise to a large scale of resulting morphologies [3,22].

Not only pure ZnO NPs are studied but also various polymer/ZnO composites attracted an attention of researchers:

polyurethane/ZnO [5], polyaniline/ZnO [7,16], poly(methyl methacrylate)/ZnO [23]. Although these nanocomposites exhibit some interesting properties, possible release of NPs from polymer into the environment represents a serious problem.

Toxicity of NPs and their potential risk to the environment and human health is still vivid and open topic and a lot of studies dealing with toxicity of ZnO NPs to plants [24], animals [25,26], and human [27] have been reported. Many other studies can be found in exhaustive and comprehensive review published recently by Ma et al. [28]. Based on the results of more than 80 works, Ma et al. concluded that ZnO NPs have toxic effects in both aquatic and terrestrial organisms (microorganisms, algae, plants, aquatic and terrestrial invertebrates, aquatic vertebrates), and for certain species, the toxicity can occur at concentrations as low as less than 1 mg dm^{-3} . This suggests that ZnO NPs, if reaching sufficient level in natural environments, can cause significant risk to the environmental biota [28].

For these serious and compelling reasons, an attention should be focused on nanocomposites in which the ZnO NPs are anchored on suitable solid matrices restricting the movement of NPs but not suppressing their unique properties.

Yang et al. [1] prepared ZnO NPs on pure Cu substrate, Collard et al. [19] synthesized SiO_2 substrate from tetraethyl orthosilicate, and Ding et al. [29] studied ZnO/graphene oxide nanocomposite but these approaches are quite expensive and used matrices cannot compete with clay minerals, i.e. layered silicates (phyllosilicates),

* Corresponding author. Tel.: +420 597 321 519.

E-mail address: jonas.tokarsky@vsb.cz (J. Tokarský).

that are abundant and widely available, chemically stable, non-toxic and very cheap.

Bentonite [17], pure montmorillonite [4,8,21], and palygorskite [20] have been successfully used for the preparation of ZnO-based nanocomposites.

However, although the kaolinite has been found as a suitable matrix for metal oxide NPs [30–32], the preparation of kaolinite/ZnO nanocomposite has been reported only by Ananthakumar et al. [13] (a mechanical mixture of kaolinite and pre-synthesized ZnO NPs).

Therefore, we decided to prepare kaolinite/ZnO nanocomposite and to test its photocatalytic activity. Using a simple hydrothermal method the composites containing 10 wt.%, 30 wt.%, and 50 wt.% of ZnO were prepared. Samples were characterized by X-ray fluorescence spectroscopy (XRFs), X-ray powder diffraction method (XRPD), Fourier transform infrared spectroscopy (FTIR), UV–VIS diffuse reflectance spectroscopy (DRS), photoluminescence spectroscopy (PLS), scanning electron microscopy (SEM), transmission electron microscopy (TEM), and BET analysis. Molecular modeling using empirical force field has been carried out in order to study structure of nanocomposite and adhesion forces between kaolinite and ZnO NPs. Photocatalytic activity of the composites was evaluated by means of photodegradation of Acid Orange 7 (AO7) model solution. AO7 exhibits the highest absorbance at the wavelength of 485 nm. This maximum corresponds to a double bond between nitrogen atoms in azo group which is cleaved first in the degradation process. Absorbance of intermediate products emerging during the AO7 degradation is minimal at the wavelength of 485 nm [33]. This fact allows direct measurement of the concentration of AO7 using VIS spectrophotometer. Therefore, an efficiency of the photocatalyst can be easily quantified.

2. Preparation and characterization methods

2.1. Preparation of the samples

ZnO NPs were synthesized by the reaction between zinc chloride (anhydrous pure, Lach-Ner, Czech Republic) and sodium hydroxide (G.R. Micropearls, Lach-Ner, Czech Republic) at the molar ratio of $\text{Zn}^{2+}:\text{OH}^-$ being 1:5. The aqueous solution of prepared zinc chloride was mixed with sodium hydroxide solution and vigorously stirred at 40 °C for 30 min. Kaolinite/ZnO nanocomposite (KAZN) was prepared by addition of the aqueous mixture of zinc chloride and sodium hydroxide solutions into the aqueous suspension of kaolinite KKAf (LB MINERALS, Czech Republic) followed by continuous stirring at 100 °C. The mixture was allowed to react for 5 h. The precursors/kaolin ratios were chosen so that the composites contained 10, 30, and 50 wt.% of ZnO. The resulting solid phase was separated by decantation, washed several times with distilled water until the conductivity of filtrate reached the value lower than $100 \mu\text{S cm}^{-1}$, and finally dried at 105 °C for 24 h [4]. Such obtained composites are denoted as KAZN1X where 1 means drying at 105 °C and X is the amount of ZnO in the sample (1 for 10 wt.%, 3 for 30 wt.%, 5 for 50 wt.%). The stability of composites was evaluated using leaching test according to the Council Decision 2003/33/EC, i.e. 10 g of composite was added into 100 ml of demineralized water, the solution was shaken for 24 h at 20 °C and, finally, the amount of released Zn was determined.

Composite was calcined at various temperatures (200–1000 °C) for 1 h. Calcined samples are denoted as KAZNTX, where T represents the calcination temperature and X has the same meaning as in the case of dried samples (i.e. the amount of ZnO). For example, KAZN65 was calcined at 600 °C and contains 50 wt.% of ZnO. Based on the results of photodegradation activity test, only dried samples and samples calcined at 600 °C were deeply characterized.

2.2. Characterization methods

2.2.1. X-ray fluorescence spectroscopy

Chemical composition of samples was determined using energy dispersive fluorescence spectrometer (XRFs) SPECTRO XEPOS (SPECTRO Analytical Instruments GmbH) equipped with 50 W Pd X-ray tube. For this measurement, samples in powder form were pressed into tablets using wax as a binder.

2.2.2. X-ray powder diffraction

X-ray powder diffraction (XRPD) patterns were recorded under $\text{CoK}\alpha$ irradiation ($\lambda = 1.789 \text{ \AA}$) using the Bruker D8 Advance diffractometer (Bruker AXS) equipped with a fast position sensitive detector VANTEC 1. Samples in powder form were pressed in a rotational holder and reflection mode was used for all measurements. Phase composition was evaluated using PDF 2 Release 2004 database (International Centre for Diffraction Data).

2.2.3. Fourier transform infrared spectroscopy

FTIR spectra were recorded in the range from 400 to 4000 cm^{-1} . Samples were measured by the ATR technique with diamond crystal on an FTIR spectrometer Nicolet 6700 (ThermoNicolet, USA).

2.2.4. UV–VIS diffuse reflectance spectroscopy

UV–VIS DRS was used for a qualitative description of the differences in the band gap shift depending on the amount of ZnO in the studied composites. UV–VIS DRS of the powder samples placed in a 5.0 mm quartz cell were registered using spectrophotometer CINTRA 303 (GBC Scientific Equipment) equipped with a reflectance sphere. Obtained reflectance spectra were transformed to Kubelka–Munk coordinates (KM) and then expressed using Tauc plot [34] showing the relation $(\text{KM} \times hf)^{1/2} = f(hf)$. Energies of band gap (E_g) were evaluated using method described in [35].

2.2.5. Photoluminescence spectroscopy

Room temperature photoluminescence spectra (PL) of KAZN samples were recorded using FLS920 (Edinburgh Instruments Ltd.) spectrometer at room temperature. Spectrometer was equipped with 450 W Xenon lamp source (excitation wavelength $\lambda = 340 \text{ nm}$). Because of high intensities of calcined samples, 395 nm filter was used for the measurement of middle part of spectra.

2.2.6. Electron microscopy

The morphology of samples was observed on a scanning electron microscope (SEM) Hitachi SU6600 (Hitachi Ltd., Japan) and a transmission electron microscope (TEM) JEOL 2010 HC (JEOL Ltd., Japan). Accelerating voltages were 5 kV and 160 kV for SEM and TEM, respectively.

2.2.7. BET analysis

Before the measurement, all samples in powder form were degassed at 105 °C for 3 h. The measurement was carried out by nitrogen adsorption in a NOVA 4000e (Quantachrome Instruments, USA) nitrogen sorption apparatus. SSA was determined by multi-point BET method using adsorption data in the relative pressure range of 0.1–0.3.

2.2.8. Evaluation of photodegradation activity

Photodegradation activity of the prepared composites was evaluated in a liquid phase, using discoloration of AO7. In order to achieve the adsorption equilibrium in the first part of the experiment, the suspension containing 0.05 g of the photocatalyst, 65 ml of demineralized water, and 5 ml of the AO7 aqueous solution ($c_0 = 6.259 \times 10^{-4} \text{ mol dm}^{-3}$) was stirred in the dark for 60 min. After 1 h of the adsorption period in the dark, the suspension was

Table 1

Chemical composition of raw kaolin KKAF and prepared composites KAZN11, KAZN13 and KAZN15 (in wt.%). LOI – loss on ignition.

Oxides	KKAF	KAZN11	KAZN13	KAZN15
Al ₂ O ₃	35.53	32.70	24.99	17.57
SiO ₂	47.74	43.18	32.88	23.10
ZnO	<0.0003	9.446	29.78	49.22
LOI	11.58	10.9	9.30	7.60

exposed to UV irradiation (UVP pen ray lamp, 365 nm). The extent of AO7 photodegradation was evaluated by the change in the intensity of absorption maximum of AO7 (480 nm) using CINTRA 303 UV–VIS spectrometer.

2.2.9. Molecular modeling

The geometry optimization of KAZN nanocomposite models and adhesion energy calculations have been carried out in the Materials Studio/Forcite module using Universal force field. Smart algorithm was used for the geometry optimization with 50,000 iterations. The atom based summation method has been used for the non-bond contributions (i.e. Coulombic and van der Waals energies) to the total potential energy. Charges were calculated using the charge equilibration (QEq) method.

3. Results and discussion

3.1. Chemical and phase composition of the samples

Chemical composition of raw kaolin KKAF and composites KAZN11, KAZN13, and KAZN15 is shown in Table 1. It is evident that the content of Al₂O₃ and SiO₂ proportionally decreases with the increase of ZnO content.

The decrease in loss on ignition (LOI) values follows the decrease of silicates amount in prepared samples.

HRPD spectra of KAZN11, KAZN13, KAZN15, and KAZN65 composites are shown in Fig. 1. Muscovite (M; PDF number 7-0042) and quartz (Q; PDF number 85-0798) represent typical mineral admixtures accompanying pure kaolinite (K; PDF number 75-1593) in kaolin KKAF. The presence of these admixtures is in good agreement with the chemical composition of the original KKAF kaolin sample. While in the chemically pure kaolinite the ideal molar ratio of SiO₂/Al₂O₃ is 2, Table 1 shows that in KKAF sample this molar ratio is ~1.34 which is caused by the above mentioned admixtures. Two characteristic reflections of kaolinite (i.e. (0 0 1) at $2\theta = 14.419^\circ$, and (0 0 2) at $2\theta = 29.043^\circ$) are maintained in all dried KAZN composites and their invariable position confirmed that ZnO does not enter the interlayer space even in large amount.

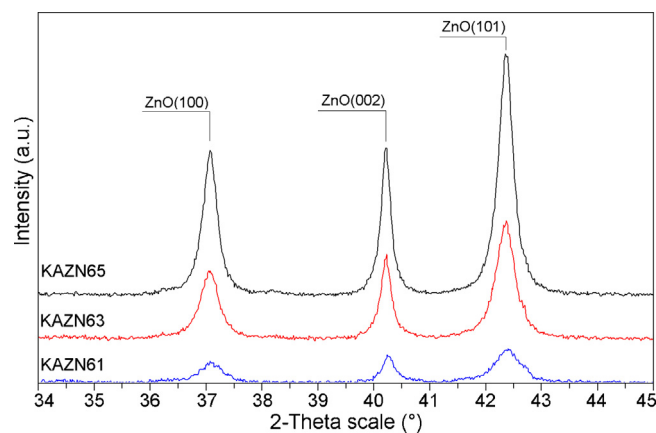


Fig. 2. The segments of diffraction patterns showing the region of ZnO(100), ZnO(002), and ZnO(101) diffraction peaks for calcined samples KAZN61, KAZN63, and KAZN65.

In the range $2\theta = 36\text{--}44^\circ$ it is evident that increasing amount of zinc oxide (ZnO; PDF number 70-2551) in KAZN11, KAZN13, KAZN15 samples and the subsequent calcination at 600°C (KAZN65 sample) led to the increased intensity of reflections and their narrowing. Detailed view can be found in Fig. 2, where (100), (002), and (101) reflections of ZnO for all three calcined composites KAZN61, KAZN63, and KAZN65 are shown. Increase of the intensity and the narrowing is caused by the recrystallization and further growth of ZnO crystallites as proved also by visual observations (see Section 3.3). The ZnO crystallite sizes (L_c) for all of the KAZN nanocomposites were calculated according to the (101) ZnO diffraction peak ($2\theta = 42.36^\circ$) using Scherrer formula [36]. Lanthanum hexaboride (LaB₆) was used as a standard and calculated L_c values for ZnO in KAZN11, KAZN13, KAZN15, KAZN61, KAZN63, and KAZN65 are 14.8 nm, 27.1 nm, 30.5 nm, 23.9 nm, 34.1 nm, and 46.2 nm, respectively.

Comparison of XRPD patterns in Fig. 1 revealed the disappearing of diffraction peaks belonging to kaolinite in calcined KAZN65 sample. According to Shvarzman et al. [37] and Fernandez et al. [38] this is the result of dehydroxylation process and subsequent kaolinite \rightarrow metakaolinite phase transformation. Taking into account that no reflections of kaolinite can be found in XRPD pattern of KAZN65

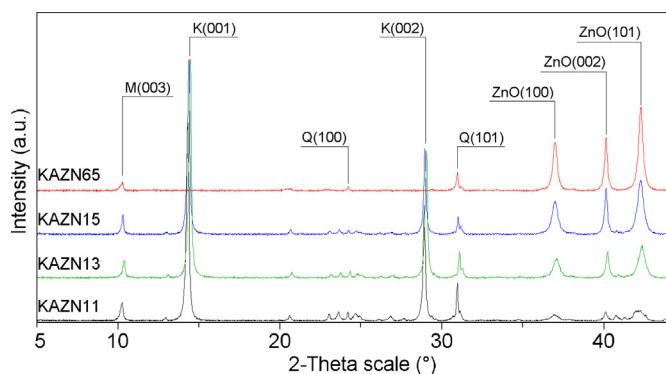


Fig. 1. XRPD pattern of samples KAZN11, KAZN13, KAZN15 (dried at 105°C), and KAZN65 (calcined at 600°C). K, kaolinite; M, muscovite; Q, quartz; ZnO, zinc oxide.

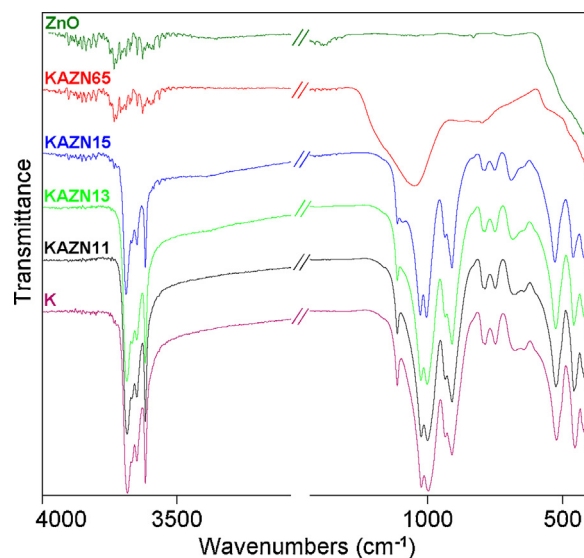


Fig. 3. FTIR spectra of kaolinite (K), ZnO NPs and KAZN nanocomposites.

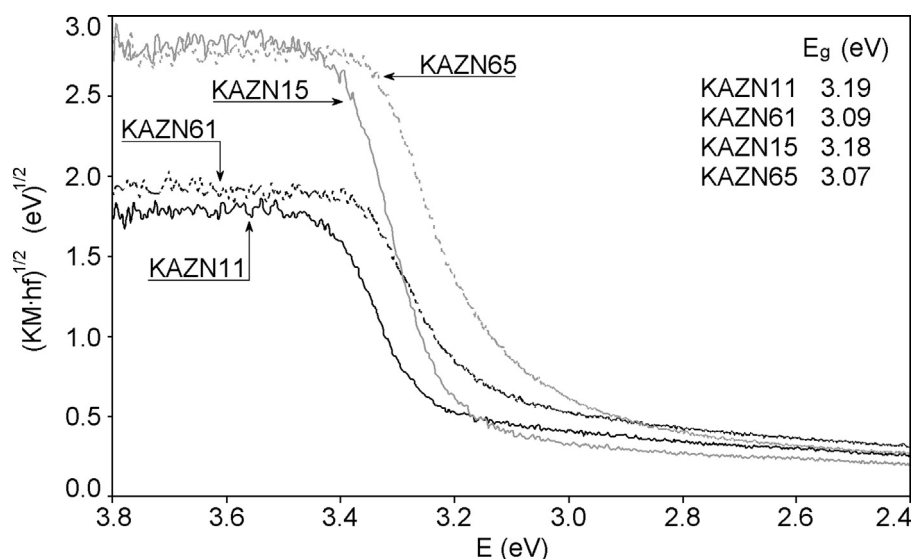


Fig. 4. UV–VIS diffuse reflectance spectra of samples KAZN11, KAZN61, KAZN15, and KAZN65.

it can be stated that after calcination at 600 °C the kaolinite was fully transformed into metakaolinite.

3.2. FTIR, DR and PL spectroscopy

FTIR studies of all samples are carried out in the region 4000–400 cm^{-1} in order to find out the changes in the kaolinite structure. The obtained ZnO spectrum is shown in Fig. 3. The Zn–O stretching vibration band with maxima at $\sim 420 \text{ cm}^{-1}$ [39] was not seen in the spectra of KAZN samples due to the overlap with the absorption bands of kaolinite. Kaolinite spectrum shows all its characteristic bands. Bands in higher wavenumbers (3668, 3650 and 3618 cm^{-1}) correspond to inner octahedral structure of Al–OH bonds and bands in lower wavenumbers correspond to following bonds: Si–O (1135, 787, 643 and 456 cm^{-1}), Si–O–Al (999, 749, 679 and 522 cm^{-1}), Al–OH (936 and 911 cm^{-1}), and Si–O–Si (1024 cm^{-1}) [40]. Spectra of samples KAZN11, KAZN13, and KAZN15 differ in wavenumbers of Si–O–Al bonds and Si–O–Si bond, which are shifted to higher values according to increasing content of ZnO in samples. This shift to the higher wavenumbers is

related to the change of the bonding characteristics, such as a bond angle [41]. Moreover, it can be seen that with increasing content of ZnO the intensity of bands related to the kaolinite decreases.

Spectrum of calcined sample KAZN65 shows typical metakaolinite spectrum, which is characteristic by diminishing of bands at higher wavenumbers belonging to O–H bonds (dehydroxylation). As a consequence of kaolinite \rightarrow metakaolinite phase transformation the Al^{3+} coordination changes from octahedral (kaolinite) to tetrahedral (metakaolinite) [40]. Broad band with maximum at 1050 cm^{-1} corresponds to the amorphous SiO_2 .

UV–VIS diffuse reflectance spectra of samples KAZN11, KAZN61, KAZN15 and KAZN65 (i.e. the samples containing the lowest and the highest amount of ZnO) are shown in Fig. 4. It is obvious that E_g values for KAZN composites are not strongly influenced by the ZnO content but the comparison of E_g values for dried (KAZN11 and KAZN15) and calcined (KAZN61 and KAZN65) samples shows the importance of calcination. The E_g values are in good agreement with photocatalytic activities of the samples, i.e. the lowest E_g (3.07 eV) was found for the sample KAZN65 exhibiting the highest photocatalytic activity (see Section 3.4).

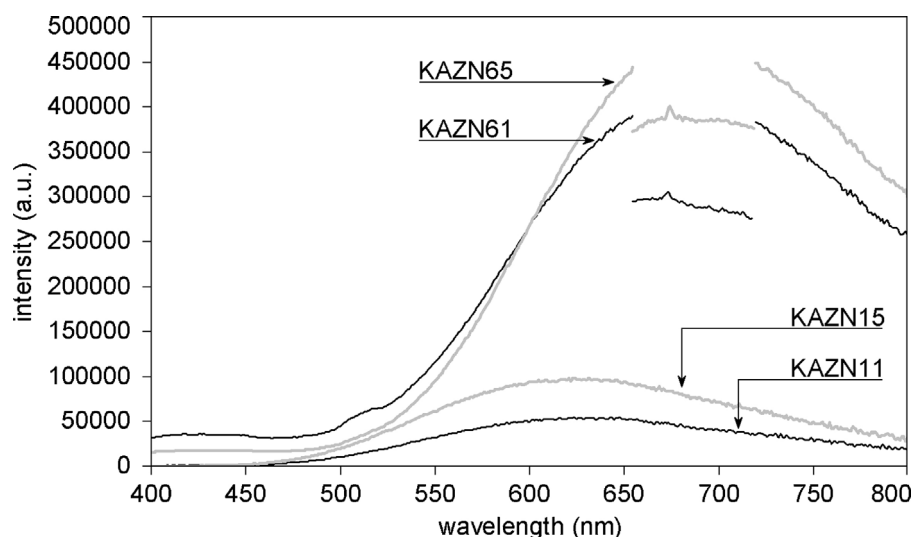


Fig. 5. Room temperature PL spectra of samples KAZN11, KAZN61, KAZN15, and KAZN65. Because of high intensities of calcined samples, 395 nm filter was used for the measurement in the region 655–720 nm.

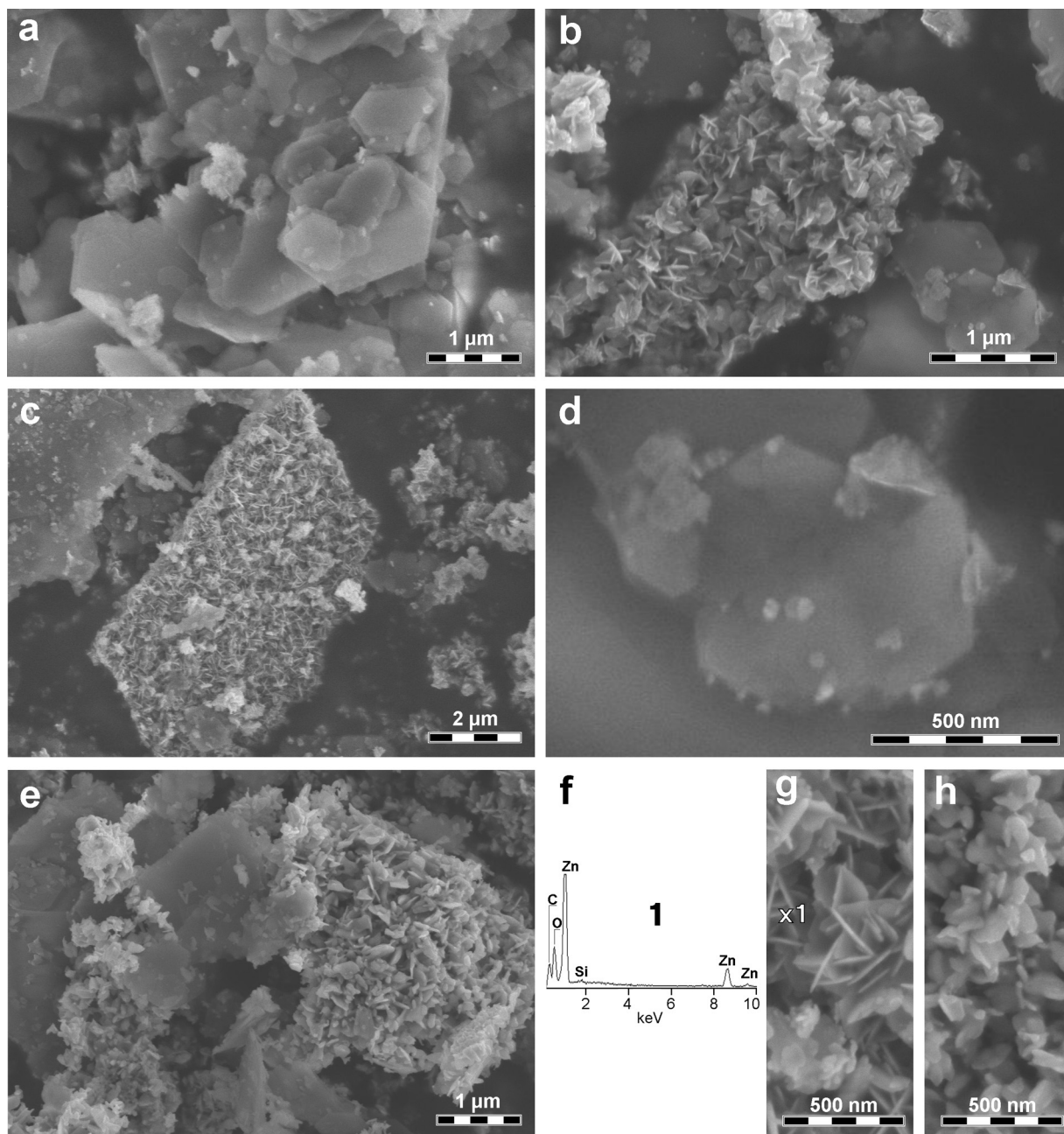


Fig. 6. SEM images of samples KAZN11 (a), KAZN13 (b, d), KAZN15 (c, g), KAZN65 (e, h), and EDS spectra obtained from KAZN15 (f).

Fig. 5 shows PL spectra of KAZN11, KAZN15, KAZN61, and KAZN65 composites. Usually, two main types of emission are observed in pure ZnO nanocrystals. The first type arises from the straight radiative recombination of the excited electron–hole pair (excitonic emission) and a relatively weak and narrow peak should be expected in the UV area with maxima close to the wavelength corresponding to E_g value. Its position is size-dependent since the energy gap between bands is affected by quantum size effect. In real defective crystal structure, another broad peak usually arises from the deep traps represented by zinc and oxygen vacancies or interstitials. These defects may act like very efficient traps for the photoexcited charge carriers and, therefore, the trap emission may be predominant or even the only radiative transition that occurs in the nanocrystal [42]. In Fig. 5 a very broad emission bands ranging from ~ 450 nm (dried samples) and ~ 500 nm (calcined samples) to near IR area can be seen. Spectra of calcined samples exhibit higher intensity and the emission maximum

is shifted to 675 nm while the maxima of dried samples can be found at 622 nm. This shift in the visible region agrees well with the enhanced photocatalytic activity of calcined samples, probably due to the larger amount of oxygen vacancies and oxygen interstitial defects. Similar observation was reported by Pudukudy and Yaakob [43,44] but unlike these studies, no UV and blue–green emissions in the area 400–500 nm were observed in case of our samples (see Fig. 5). Therefore, it can be assumed that vacancies and interstitial defects play a dominant role in the emission properties of KAZN samples.

3.3. Morphology of prepared composites

Morphology of the composites was studied using electron microscopy and SEM micrographs are shown in Fig. 6. One can see that there are not many ZnO NPs in the KAZN11 composite and the kaolinite matrix is quite empty (Fig. 6a). However, increasing

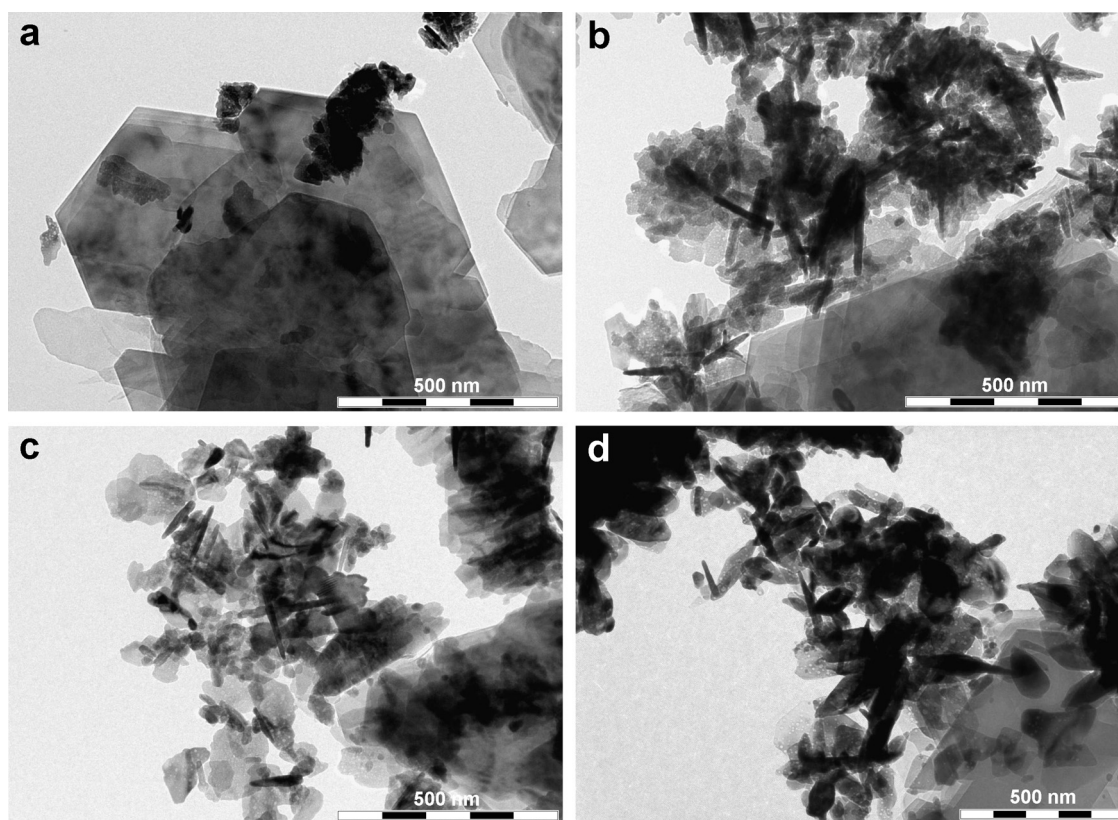


Fig. 7. TEM images of samples KAZN11 (a), KAZN13 (b), KAZN15 (c), and KAZN65 (d).

amount of ZnO is accompanied with formation of larger NPs and both Fig. 6b (KAZN13) and Fig. 6c (KAZN15) show the kaolinite particles covered by continuous layer of ZnO NPs. For EDS spectra of ZnO see Fig. 6f. Shape of these NPs is very similar to the shape of macroscopic crystals of gypsum (the so-called “desert rose”). The same shape was reported by Xu et al. [3] and due to the use of the same precursor, i.e. ZnCl_2 , the accordance is understandable. However, quite similar shapes of ZnO NPs were obtained also using $\text{Zn}(\text{NO}_3)_2$ [2] or $\text{Zn}(\text{Ac})_2$ [19].

Except large ZnO NPs also smaller ones can be found in samples and these small NPs grow on kaolinite edges (Fig. 6d). Calcined sample KAZN65 contains large ZnO NPs growing on flat kaolinite surface similarly as in the KAZN15 composite, i.e. the calcination at 600°C did not destroy the continuous layers of ZnO NPs (Fig. 6e). It can be clearly seen that slices of ZnO in the KAZN65 sample are thicker than in dried samples. This difference comes from the growth of ZnO crystallites during the calcination process as discussed in Section 3.1. Comparison of ZnO NPs in dried and calcined composites is shown in Fig. 6g (KAZN15) and Fig. 6h (KAZN65).

TEM analysis was used to observe the internal structure of ZnO NPs (Fig. 7). Sample KAZN11 contains only few small NPs with indistinguishable structure (Fig. 7a) but in case of KAZN13 (Fig. 7b) and KAZN15 (Fig. 7c) it is evident that ZnO NPs are created by clusters of crystallites having the form of larger or smaller slices. Comparison of their size with image scale shows good agreement with L_c values calculated from XRPD diffractograms in Section 3.1. TEM analysis also confirmed the thicker crystallites in KAZN65 composite (compare Fig. 7b and c with Fig. 7d).

Specific surface area (SSA) of calcined composites was estimated using BET analysis. It was found that SSA increases with increasing amount of ZnO NPs as follows: $6.54\text{ m}^2\text{ g}^{-1}$ (KAZN61), $7.34\text{ m}^2\text{ g}^{-1}$ (KAZN63), and $13.47\text{ m}^2\text{ g}^{-1}$ (KAZN65). This increase is in good agreement with ZnO crystallite sizes listed in Section 3.1.

3.4. Photodegradation activity

In order to find a calcination temperature leading to the highest photodegradation activity of resulting composite, set of five samples calcined at 300°C , 500°C , 600°C , 800°C , and 1000°C for 1 h was tested. Composite with the highest amount of ZnO (i.e. KAZN15) was chosen for this experiment in order to obtain a demonstrable effect of calcination temperature on ZnO NPs. Results are shown in Fig. 8 and one can see that the highest photodegradation activity (95%) was reached in the case of KAZN65. Therefore, calcination temperature 600°C was further used also for KAZN11 and KAZN13 composites.

The comparison of KAZN1X and KAZN6X in Fig. 9 clearly shows the effect of calcination temperature on photodegradation activity.

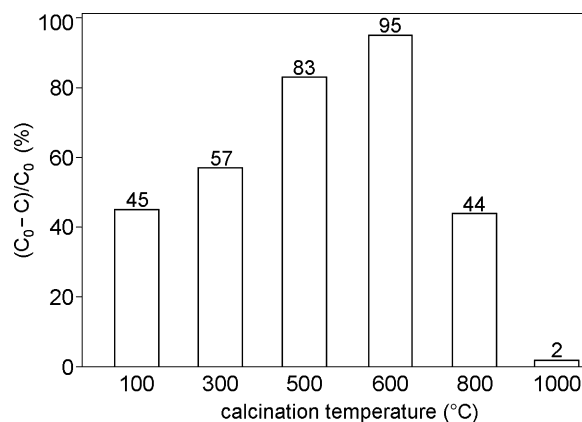


Fig. 8. Photodegradation activity of KAZN15 composite, dried and calcined at various temperatures.

Table 2

Experimental data from various photodegradation tests using ZnO as the photoactive component. Model pollutants (mod. pollut.) AO7, CR, MO, MB, and RhB are Acid Orange 7, Congo Red, Methyl Orange, Methylene Blue, and Rhodamine B, respectively. Values of initial concentration of model pollutant (c_0), volume of solution (V_s), amount of photocatalyst in the solution ($\rho_{\text{photocat.}}$), amount of ZnO in photocatalyst (w_{ZnO}), irradiation time (t) and degradation efficiency (Φ) are listed. The abbreviation n.p. means not provided.

Mod. pollut.	c_0 (mol dm ⁻³)	V_s (dm ³)	$\rho_{\text{photocat.}}$ (g dm ⁻³)	w_{ZnO} (wt.%)	Irradiation (wavelength)	t (min)	Φ (%)	Ref.
AO7	4.471×10^{-5}	0.07	0.7	50	UV (365 nm)	60	95	Present work
AO7	1×10^{-3}	0.25	n.p.	>95	Sunlight	100	97	[45]
CR	6×10^{-5}	0.04	2.5	~88	UV (n.p.)	60	92	[6]
CR	9×10^{-5}	0.04	2.5	~88	UV (n.p.)	60	89	[6]
CR	1×10^{-4}	0.04	2.5	~88	UV (n.p.)	60	86	[6]
MO	1.0×10^{-4}	0.3	2	~100	UV (470 nm)	20	18	[12]
MO	1.0×10^{-4}	0.3	2	~100	VIS (420 nm)	20	16	[12]
MB	4×10^{-5}	0.1	1	98	VIS (n.p.)	50	100	[18]
MB	1.563×10^{-5}	0.05	1	100	UV (n.p.)	60	98	[11]
MB	6.253×10^{-5}	0.05	1	100	UV (n.p.)	60	98	[11]
MB	7.816×10^{-5}	0.05	1	100	UV (n.p.)	60	95	[11]
MB	9.379×10^{-5}	0.05	1	100	UV (n.p.)	60	88	[11]
MB	3.126×10^{-5}	0.25	0.2	5	VIS (663 nm)	30	80	[8]
MB	3.126×10^{-5}	0.25	0.2	5	VIS (663 nm)	150	97	[8]
MB	3.126×10^{-5}	0.1	2	0.5	VIS (n.p.)	160	76	[16]
MB	6.4×10^{-6}	0.075	0.4	~100	UV (200–400 nm)	100	84	[13]
RhB	2×10^{-5}	0.05	1	100	UV (360 nm)	180	92	[19]
Phenol	1.062×10^{-2}	1	0.3	~10	UV (365 nm)	120	67	[17]
Phenol	2.125×10^{-3}	1	0.3	~10	UV (365 nm)	120	80	[17]

After 1 h of UV irradiation, 80% of AO7 was degraded by KAZN61 composite and with increasing content of ZnO the photodegradation efficiency reached 93% and 95% in case of KAZN63 and KAZN65, respectively. It can be also observed that dried KAZN13 composite exhibits lower photodegradation activity than KAZN15 composite but after calcination at 600 °C the activities are nearly the same (Fig. 9).

Significantly higher photoactivity of calcined samples is in good agreement with other analyses. ZnO crystallites are larger after the calcination process ($L_c(\text{KAZN15}) = 30.5$ nm, $L_c(\text{KAZN65}) = 46.2$ nm; see Section 3.1), the E_g energies are lower ($E_g(\text{KAZN15}) = 3.18$ eV, $E_g(\text{KAZN65}) = 3.07$ eV; see Fig. 4), and maxima of emission bands are shifted in the VIS region ($\lambda_{\text{max}}(\text{KAZN15}) = 622$ nm, $\lambda_{\text{max}}(\text{KAZN65}) = 675$ nm; see Fig. 5). Also the SSA of KAZN65 composite (13.47 m² g⁻¹) is larger than KAZN61 and KAZN63 composites (6.54 m² g⁻¹ and 7.34 m² g⁻¹).

Time dependence of AO7 degradation on irradiation time for KAZN65 composite is displayed in Fig. 10. Only 5% of AO7 remained in the solution after 60 min of irradiation and after 30 min more than 60% was degraded.

Table 2 summarizes data from various photodegradation experiments published by other authors. Unfortunately, different experimental conditions (type of model pollutant, concentration, irradiation wavelength and time, amount of photocatalyst, etc.) do not allow the direct comparison but still some conclusions with regard to KAZN composite can be made.

Ag-doped ZnO studied by Shinde et al. [45] has very high degradation activity even the concentration of AO7 was two orders of magnitude higher than ours. Nevertheless, the photocatalyst is nearly pure ZnO and the amount used in the experiment is not provided.

Broadly the same concentration of Congo Red was used by Chandraboss et al. [6]. More than three times higher amount of photocatalyst (~88 wt.% of ZnO) was used but the degradation efficiency is lower.

Graphene oxide/ZnO nanocomposite studied by Wang et al. [18] exhibits excellent photodegradation activity against methylene blue (MB). The concentration of pollutant, volume of solution, amount of photocatalyst and irradiation time are very similar to our experiment. Wang et al. reached complete degradation (100%) of MB after 50 min of irradiation. However, the amount of ZnO was two times higher than in our experiment.

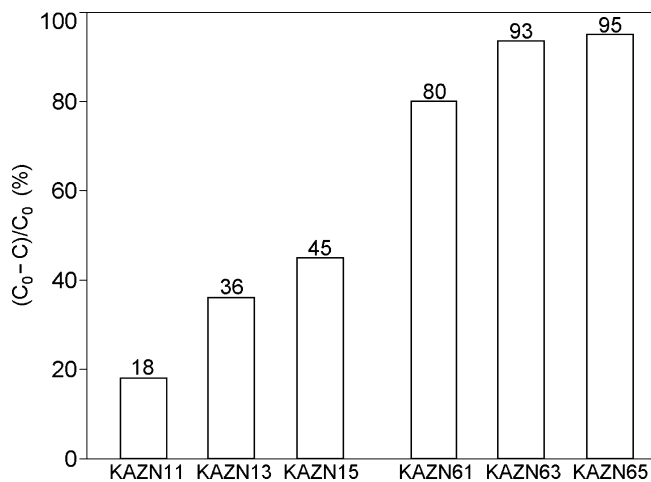


Fig. 9. Photodegradation activity of composites containing 10, 30, and 50 wt.% of ZnO, dried at 105 °C (KAZN11, KAZN13, KAZN15) and calcined at 600 °C (KAZN61, KAZN63, KAZN65).

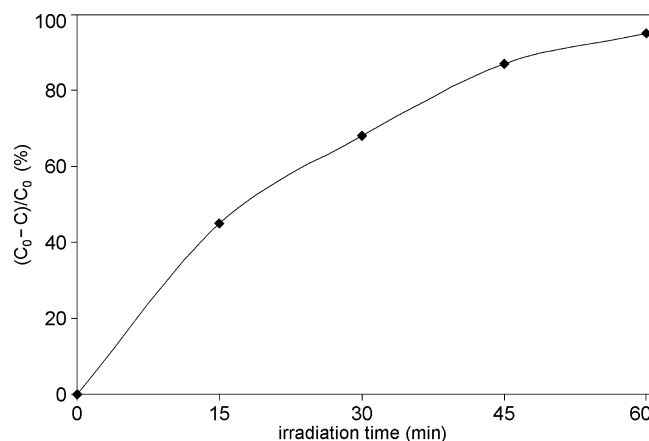


Fig. 10. Photodegradation of AO7 in dependence on irradiation time for sample KAZN65.

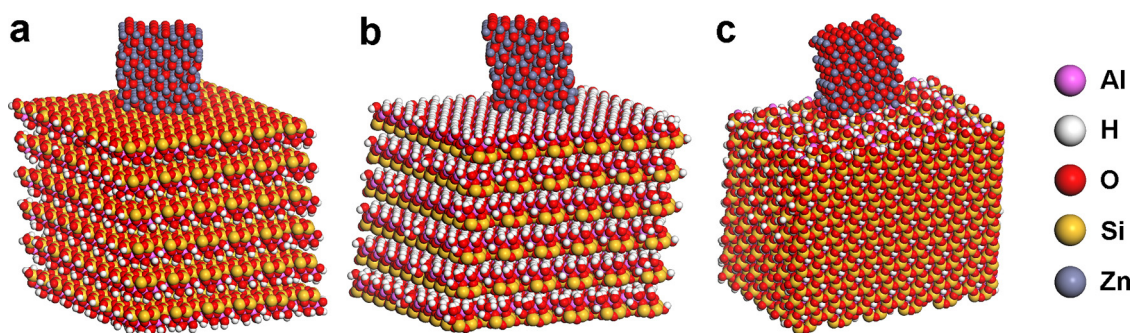


Fig. 11. Optimized models of large ZnO(001) NP anchored on tetrahedral surface (a), octahedral surface (b), and edge (c) of the KLT matrix.

The most valuable results for our comparison were reported by Pudukudy and Yaakob [11] because the experimental conditions were the most similar to our work, although the MB was used and the wavelength of UV light is not provided. Pudukudy and Yaakob used pure ZnO (i.e. two times higher amount) and after the same time of irradiation (60 min) the photodegradation efficiency was 95% in average. Our composite KAZN65 contains 50 wt.% of ZnO, NPs are anchored on kaolinite matrix and the photodegradation efficiency is also 95%. This is a good confirmation of the fact that KAZN is very efficient photocatalyst.

Photodegradation efficiency of montmorillonite/ZnO(5.0 wt.%) nanocomposite prepared by Fatimah et al. [8] reached 97% after two and half times longer time. Moreover, the photoactivity was tested in presence of H_2O_2 . This nanocomposite cannot compete with KAZN and polyaniline/ZnO(0.5 wt.%) nanocomposite [16] also not.

KAZN also exhibits higher photodegradation activity than ZnO NPs tested by Ananthakumar et al. [13]) and Collard et al. [19].

Comparison with the results of Meshram et al. [17] is problematic due to the significantly higher concentrations of model pollutant (phenol).

3.5. Molecular modeling

Molecular modeling using empirical force field as implemented in Materials Studio modeling environment has been used to study the structure of the KAZN nanocomposite and the adhesion forces between ZnO NPs and the kaolinite matrix. The structure of real kaolinite was approximated by $(\text{Al}_8)(\text{Si}_8)\text{O}_{20}(\text{OH})_{16}$ and the model of kaolinite matrix was built as a non-periodic superstructure containing six layers (see Fig. 11). The total crystallochemical formula of resulting model is $(\text{Al}_{1254})(\text{Si}_{1296})\text{O}_{3156}(\text{OH})_{2640}$, the size is $5.1 \text{ nm} \times 4.4 \text{ nm}$ and thickness $\sim 4.1 \text{ nm}$. Distance between layers (i.e. basal spacing) 0.74 nm corresponds to the real structure of kaolinite [46]. No tetrahedral cationic substitutions are present in this idealized model and the total layer charge of -6 el. comes fully from the non-stoichiometry on the edges. This layer charge is compensated by the anchored ZnO NP. QEq (charge equilibration) method has been used to calculate the atomic charges of kaolinite and NPs [47].

Six types of ZnO NPs with crystallographic orientations (001), (100), and (101) have been prepared in two sizes, $\text{Zn}_{92}\text{O}_{89}$ and $\text{Zn}_{186}\text{O}_{183}$. The charge of each NP is $+6 \text{ el.}$ and in order to ensure the similarity of NPs for possible comparison of obtained results, each NP has 20 Zn atoms in the plane adjacent to the kaolinite. Because the distribution of atoms is different in various hkl planes, each NP has a different surface area S : 1.47 nm^2 (001), 2.03 nm^2 (100), and 1.08 nm^2 (101).

Initial models have been prepared by anchoring each NP to one of the three possible types of kaolinite matrix, i.e. tetrahedral surface (basal SiO surface; see Fig. 11a), octahedral surface (basal

Table 3

Adhesion energies per surface area between ZnO NP and kaolinite matrix are summarized in dependence on size of NP, location and (hkl) indices of ZnO adjacent plane.

Size of NP	Location	E_{ad} ($\text{kJ mol}^{-1} \text{Å}^{-2}$)		
		ZnO(001)	ZnO(100)	ZnO(101)
$\text{Zn}_{92}\text{O}_{89}$	SiO surface	140	71	140
	OH surface	167	89	190
	Edge	149	126	203
	SiO surface	154	206	336
$\text{Zn}_{186}\text{O}_{183}$	OH surface	150	190	253
	Edge	114	154	173

OH surface; see Fig. 11b), and edge (see Fig. 11c). The interaction between the ZnO NP and the kaolinite matrix was quantified using the adhesion energy per surface area.

$$E_{\text{ad}} = \frac{(E_{\text{tot,ZnO}} + E_{\text{tot,K}}) - E_{\text{tot}}}{S} \quad (1)$$

where E_{tot} is the total energy of the nanocomposite (i.e. the ZnO NP anchored on the kaolinite matrix). $E_{\text{tot,ZnO}}$ is the total energy of ZnO NP, and $E_{\text{tot,K}}$ is the total energy of the kaolinite matrix. The higher value of E_{ad} the strongest adhesion between NP and kaolinite surface. These energies are expressed in the unit $[\text{kcal mol}^{-1} \text{Å}^{-2}]$ and have been calculated in Materials Studio/Forcite module using the Universal force field [48] which was successfully used for the similar types of models in our previous works [30,31,49].

Adhesion energies per surface area are summarized in Table 3 and based on these E_{ad} values two following conclusion can be made. (1) While small NPs prefer the kaolinite edge, for larger NPs it is the least favorable location and 001 surfaces of kaolinite are preferred. This result is in good agreement with visual observation of SEM images where only very small ZnO NPs were found on kaolinite edges (Fig. 6d). (2) The most preferred ZnO plane is (101). Regardless of the NP size and location, all models containing ZnO(101) NP exhibit the highest adhesion energy. There is only one exception: see the first line of Table 3 and slightly higher E_{ad} for the ZnO(001) plane. This result suggests that ZnO NPs adhere to the kaolinite via (101) plane.

3.6. Leaching tests

Leaching tests carried out according to the Council Decision 2003/33/EC showed that ZnO NPs are strongly anchored on the kaolinite matrix. Only negligible amount of Zn was released from nanocomposites after 24 h of shaking in demineralized water: 10.6 mg dm^{-3} (KAZN11), 4.14 mg dm^{-3} (KAZN13), and 1.46 mg dm^{-3} (KAZN15). Amounts of released Zn do not reach the limit value 15 mg dm^{-3} and, therefore, all composites may be considered non-hazardous. Moreover, amount of Zn released from

KAZ15 composite is approaching the value 1.2 mg dm^{-3} specified in the Council Decision 2003/33/EC as a limit for inert materials.

4. Conclusions

Simple and cheap hydrothermal method was used to prepare ZnO NPs growing on kaolinite particles. Preparation conditions (kaolinite:ZnO ratio and calcination temperature) were optimized in order to reach the highest photocatalytic activity. The optimum was found to be 50 wt.% of ZnO and 600°C . X-ray diffraction analysis revealed that ZnO do not enter the interlayer space of kaolinite and that the average size of ZnO crystallites is about 46 nm. Visual observations supported by molecular modeling proved the preferential growth of ZnO NPs on kaolinite (001) surfaces and not on the edges. Results of molecular modeling also suggest that ZnO NPs adhered to the kaolinite surface via ZnO(101) planes.

Calcination at 600°C led to the shift of DR spectra and maxima of emission bands in PL spectra in the visible region and, therefore, to the significant increase of photodegradation efficiency which for the nanocomposite containing 50 wt.% of ZnO reached 95% after UV irradiation for 1 h. Moreover, PL spectra revealed the existence of oxygen vacancies and interstitial defects on the surface of calcined ZnO NPs.

Although the photodegradation efficiency of KAZN63 is slightly lower (93%), it is still sufficiently high. It means that also lower amounts of ZnO NPs (30–50 wt.%) can be used for the preparation of photoactive nanocomposites.

Kaolinite \rightarrow metakaolinite phase transformation occurring during calcination is also important because of latent hydraulic properties exhibited by metakaolinite. Presence of metakaolinite may be an advantage for using this nanocomposite in building industry.

Leaching tests confirmed that kaolinite/ZnO nanocomposites may be considered non-hazardous.

The main and the most important result of present work is the evidence that anchoring of ZnO NPs on kaolinite matrix restricts the release of Zn into the environment but do not suppress the photocatalytic properties of NPs.

Acknowledgments

This work was supported by the European Regional Development Fund in the IT4Innovations Centre of Excellence (project reg. no. CZ.1.05/1.1.00/02.0070) and by the Ministry of Education, Youth and Sports of Czech Republic (project reg. no. SP2014/52). The authors would like to thank Lucie Neuwirthová for the determination of chemical composition using XRFs, Soňa Študentová for BET analyses, Ladislav Svoboda for PL spectra, and Klára Šafářová (Regional Centre of Advanced Technologies and Materials, Faculty of Science, Palacky University in Olomouc) for SEM and TEM measurements.

References

- [1] J. Yang, J. Zheng, H. Zhai, X. Yang, L. Yang, Y. Liu, J. Lang, M. Gao, *J. Alloys Compd.* 489 (2010) 51–55.
- [2] J. Huang, Y. Wu, C. Gu, M. Zhai, Y. Sun, J. Liu, *Sens. Actuators B* 155 (2011) 126–133.

- [3] X. Xu, H. Pang, Z. Zhou, X. Fan, S. Hu, Y. Wang, *Adv. Powder Technol.* 22 (2011) 634–638.
- [4] N. Khaorapapong, N. Khumchoo, M. Ogawa, *Mater. Lett.* 65 (2011) 657–660.
- [5] J.H. Li, R.Y. Hong, M.Y. Li, H.Z. Li, Y. Zheng, J. Ding, *Prog. Org. Coat.* 64 (2009) 504–509.
- [6] V.L. Chandraboss, L. Natanapatham, B. Karthikeyan, J. Kamalakkannan, S. Prabha, S. Senthilvelan, *Mater. Res. Bull.* 48 (2013) 3707–3712.
- [7] B.K. Sharma, A.K. Gupta, N. Khare, S.K. Dhawan, H.C. Gupta, *Synth. Met.* 159 (2009) 391–395.
- [8] I. Fatimah, S. Wang, D. Wulandari, *Appl. Clay Sci.* 53 (2011) 553–560.
- [9] R. Wahab, Y.-S. Kim, I.H. Hwang, H.-S. Shin, *Synth. Met.* 159 (2009) 2443–2452.
- [10] D. Sebők, K. Szendrei, T. Szabó, I. Dékány, *Thin Solid Films* 516 (2008) 3009–3014.
- [11] M. Pudukudy, Z. Yaakob, *Appl. Surf. Sci.* 292 (2014) 520–530.
- [12] C. Shifu, Z. Wei, Z. Sujuan, L. Wei, *Chem. Eng. J.* 148 (2009) 263–269.
- [13] S. Ananthakumar, S. Anas, J. Ambily, R.V. Mangalaraja, *J. Ceram. Process. Res.* 11 (2010) 164–169.
- [14] J. Liu, X. Chen, W. Wang, Y. Liu, Q. Huang, Z. Guo, *Cryst. Eng. Commun.* 13 (2011) 3425–3431.
- [15] J. Xie, P. Li, Y. Wang, Y. Wei, *J. Phys. Chem. Sol.* 70 (2009) 112–116.
- [16] S. Ameen, M.S. Akhtar, Y.S. Kim, O.-B. Yang, H.-S. Shin, *Colloid. Polym. Sci.* 289 (2011) 415–421.
- [17] S. Meshram, R. Limaye, S. Ghodke, S. Nigam, S. Sonawane, R. Chikate, *Chem. Eng. J.* 172 (2011) 1008–1015.
- [18] X. Wang, L. Zhou, F. Li, *New Carbon Mater.* 28 (2013) 408–413.
- [19] X. Collard, M. El Hajji, B.-L. Su, C. Aprile, *Microporous Mesoporous Mater.* 184 (2014) 90–96.
- [20] C. Huo, H. Yang, *Appl. Clay Sci.* 50 (2010) 362–366.
- [21] Y.-L. Ma, B. Yang, L. Xie, *Colloids Surf. B* 79 (2010) 390–396.
- [22] J. Chang, M.Z. Ahmad, W. Włodarski, E.R. Wacławik, *Sensors* 13 (2013) 8445–8460.
- [23] A. Laachachi, D. Ruch, F. Addiego, M. Ferriol, M. Cochez, J.-M. Lopez Cuesta, *Polym. Degrad. Stab.* 94 (2009) 670–678.
- [24] S. Rao, G.S. Shekhawat, *J. Environ. Chem. Eng.* 2 (2014) 105–114.
- [25] X. Zhao, S. Wang, Y. Wu, H. You, L. Lv, *Environ. Pollut.* 172 (2013) 76–85.
- [26] N. Santo, U. Fascio, F. Torres, N. Guazzoni, P. Tremolada, R. Bettinetti, P. Mantecchia, R. Bacchetta, *Water Res.* 53 (2014) 339–350.
- [27] B.C. Heng, X. Zhao, S. Xiong, K.W. Ng, F.Y.-C. Boey, J.S.-C. Loo, *Food Chem. Toxicol.* 48 (2010) 1762–1766.
- [28] H. Ma, P.L. Williams, S.A. Diamond, *Environ. Pollut.* 172 (2013) 76–85.
- [29] L. Ding, Z.E.L. Fan, S. Yang, *Chem. Commun.* 49 (2013) 6286–6288.
- [30] K. Mamulová Kutláková, J. Tokarský, P. Kovář, S. Vojtěšková, A. Kovářová, B. Smetana, J. Kukutschová, P. Čapková, V. Matějka, *J. Hazard. Mater.* 188 (2011) 212–220.
- [31] J. Tokarský, P. Čapková, J.V. Burda, *J. Mol. Model.* 18 (2012) 2689–2698.
- [32] V. Matějka, P. Matějková, P. Kovář, J. Vlček, J. Příkryl, P. Červenka, Z. Lacný, J. Kukutschová, *Constr. Build. Mater.* 35 (2012) 38–44.
- [33] I.K. Konstantinou, T.A. Albanis, *Appl. Catal. B* 49 (2004) 1–14.
- [34] J. Tauc, R. Grigorovici, A. Vancu, *Phys. Status Solidi* 15 (1966) 627–637.
- [35] K. Kočí, L. Obalová, L. Matějová, D. Plachá, Z. Lacný, J. Jirkovský, O. Šolcová, *Appl. Catal. B* 89 (2009) 494–502.
- [36] P. Scherrer, *Nachr. Ges. Wiss. Göttingen* (1918).
- [37] A. Shvarzman, K. Kovler, G.S. Grader, G.E. Shter, *Cem. Concr. Res.* 3 (2003) 405–416.
- [38] R. Fernandez, F. Martirena, K.L. Scrivener, *Cem. Concr. Res.* 41 (2011) 113–122.
- [39] K.G. Chandrappa, T.V. Venkatesha, K. Vathsala, C. Shivakumara, *J. Nanopart. Res.* 12 (2010) 2667–2678.
- [40] H.W. van der Marel, H. Beutelspacher, *Atlas of Infrared Spectroscopy of Clay Minerals and their Admixtures*, Elsevier Science Ltd, Amsterdam, 1976.
- [41] Y.-H. Kim, M.S. Hwang, H.J. Kim, *J. Appl. Phys.* 90 (2001) 3367–3370.
- [42] A. van Dijken, E.A. Meulenlamp, D. Vanmaekelbergh, A. Meijerink, *J. Lumin.* 87–89 (2000) 454–456.
- [43] M. Pudukudy, Z. Yaakob, *Superlattices Microstruct.* 63 (2013) 47–57.
- [44] M. Pudukudy, Z. Yaakob, *Solid State Sci.* 30 (2014) 78–88.
- [45] S.S. Shinde, C.H. Bhosale, K.Y. Rajpure, *J. Photochem. Photobiol. B* 117 (2012) 262–268.
- [46] R.B. Neder, M. Burghammer, T. Grasl, H. Schulz, A. Bram, S. Fiedler, *Clays Clay Miner.* 47 (1999) 487–494.
- [47] A.K. Rappe, W.A. Goddard, *J. Phys. Chem.* 95 (1991) 3358–3363.
- [48] A.K. Rappe, C.J. Casewit, K.S. Colwell, W.A. Goddard, W.M. Skiff, *J. Am. Chem. Soc.* 114 (1992) 10024–10035.
- [49] J. Tokarský, V. Matějka, L. Neuwirthová, J. Vontorová, K. Mamulová Kutláková, J. Kukutschová, P. Čapková, *Chem. Eng. J.* 222 (2013) 488–497.